

Dust changes in Sakurai’s Object: new PAHs and SiC with coagulation of submicron-sized silicate dust into 10 μ m-sized melilite grains

Janet E. Bowey¹★

¹ *School of Physics and Astronomy, Cardiff University, Queens Buildings, The Parade, Cardiff CF24 3AA, UK.*

Accepted XXX. Received YYY; in original form ZZZ

ABSTRACT

6–14 μ m Spitzer spectra obtained at 6 epochs between April 2005 and October 2008 are used to determine temporal changes in dust features associated with Sakurai’s Object (V4334 Sgr), a low mass post-AGB star that has been forming dust in an eruptive event since 1996. The obscured carbon-rich photosphere is surrounded by a 40-milliarcsec torus and 32 arcsec PN. An initially rapid mid-infrared flux decrease stalled after 21 April 2008. Optically-thin emission due to nanometre-sized SiC grains reached a minimum in October 2007, increased rapidly between 21–30 April 2008 and more slowly to October 2008. 6.3- μ m absorption due to PAHs increased throughout. 20 μ m-sized SiC grains might have contributed to the 6–7 μ m absorption after May 2007. Mass estimates based on the optically-thick emission agree with those in the absorption features if the large SiC grains formed before May 1999 and PAHs formed in April–June 1999. Estimated masses of PAH and large-SiC grains in October 2008, were $3 \times 10^{-9} M_{\odot}$ and $10^{-8} M_{\odot}$, respectively. Some of the submicron-sized silicates responsible for a weak 10 μ m absorption feature are probably located within the PN because the optical depth decreased between October 2007 and October 2008. 6.9 μ m absorption assigned to ~ 10 μ m-sized crystalline melilite silicates increased between April 2005 and October 2008. Abundance and spectroscopic constraints are satisfied if $\lesssim 2.8$ per cent of the submicron-sized silicates coagulated to form melilites. This figure is similar to the abundance of melilite-bearing calcium-aluminium-rich inclusions in chondritic meteorites.

Key words: stars: AGB and post-AGB < Stars, (stars:) circumstellar matter < Stars, stars: carbon < Stars, (ISM:) dust, extinction < Interstellar Medium (ISM), Nebulae, stars: individual:... < Stars, stars: evolution < Stars

1 INTRODUCTION

Sakurai’s Object (V4334 Sgr) is a low mass post-AGB star that is undergoing a very late thermal pulse caused by the ignition of a residual helium shell. It has formed substantial quantities of dust during the 25 years since its discovery by Yukio Sakurai in 1996 (Nakano et al. 1996). The source was later identified ($V \sim 12.5$ mag) in pre-discovery optical images from January 1995; it brightened to 11.4 mag in the first 12 months and showed no nova-like emission lines. In March 1996 the photosphere was hydrogen-poor with over abundances of carbon and oxygen and centred in a 32'' circular planetary nebula (Duerbeck & Benetti 1996). Once the photosphere was obscured CN, C₂ and CO were detected in its atmosphere (Eyres et al. 1998). Later infrared observations revealed HCN and C₂H₂ with ¹²C to ¹³C isotope ratios which are consistently lower than the Solar System values; (see Evans et al. 2020, hereinafter Ev2020, for a detailed history). Like other ‘Born Again Giants’ it lies at the centre of an older faint planetary nebula (PN) (Pollacco 1999). Chesneau et al. (2009) obtained high spatial-resolution 7.5–13.5 μ m observations in June 2007 and deduced that the star was surrounded by a 30 \times 40 milliarcsec opaque dusty disc or torus inclined at 75 deg to the plane of the sky and aligned with a low level of asymmetry seen in the old PN. The source continues to evolve and the 2015–2019 expansion

of the bipolar nebula has recently been mapped in the near-infrared by Hinkle et al. (2020) and images show the existence of 760 K dust which are likely to be a consequence of a near-IR brightening event observed in 2008 (e.g. Hinkle & Joyce 2014).

To date the dust mineralogy has not been studied in much detail; this work is focussed on Ev2020’s reporting of a weak, but consistent, absorption feature with minima at 6.3 μ m and 6.9 μ m (Figure 1) in their low-resolution Spitzer spectra of the source which they tentatively attributed to hydrogenated amorphous carbon (HAC) formed in an early mass ejection phase prior to 1997. These features resemble part of similar absorption bands in dense cold ($\lesssim 100$ K) lines of sight through young stellar objects (YSOs) and molecular clouds (e.g. Keane et al. 2001; Boogert et al. 2011) which are normally associated with a combination of ices, carbonaceous material, carbonates, or occasionally with overtone bands of a crystalline silicate called melilite (Bowey & Hofmeister 2005). Overtone bands are 1/100th the strength of fundamental bands like the 10 μ m Si-O stretch and are therefore seen only in samples where the fundamental bands are opaque due to larger grain sizes or in micron to 100 μ m-thick films of finely-ground powders. Since the grain density in YSO discs is extremely high (Bowey & Hofmeister 2005) did not make the connection with large grain sizes or coagulated grains producing the features. In Sakurai’s Object the absence of evidence for H₂O ice at 3.0 μ m and 6.0 μ m in the currently oxygen-poor environment means that H₂O and other ices and carbonates (which are not known to form

★ E-mail: boweyj@cardiff.ac.uk

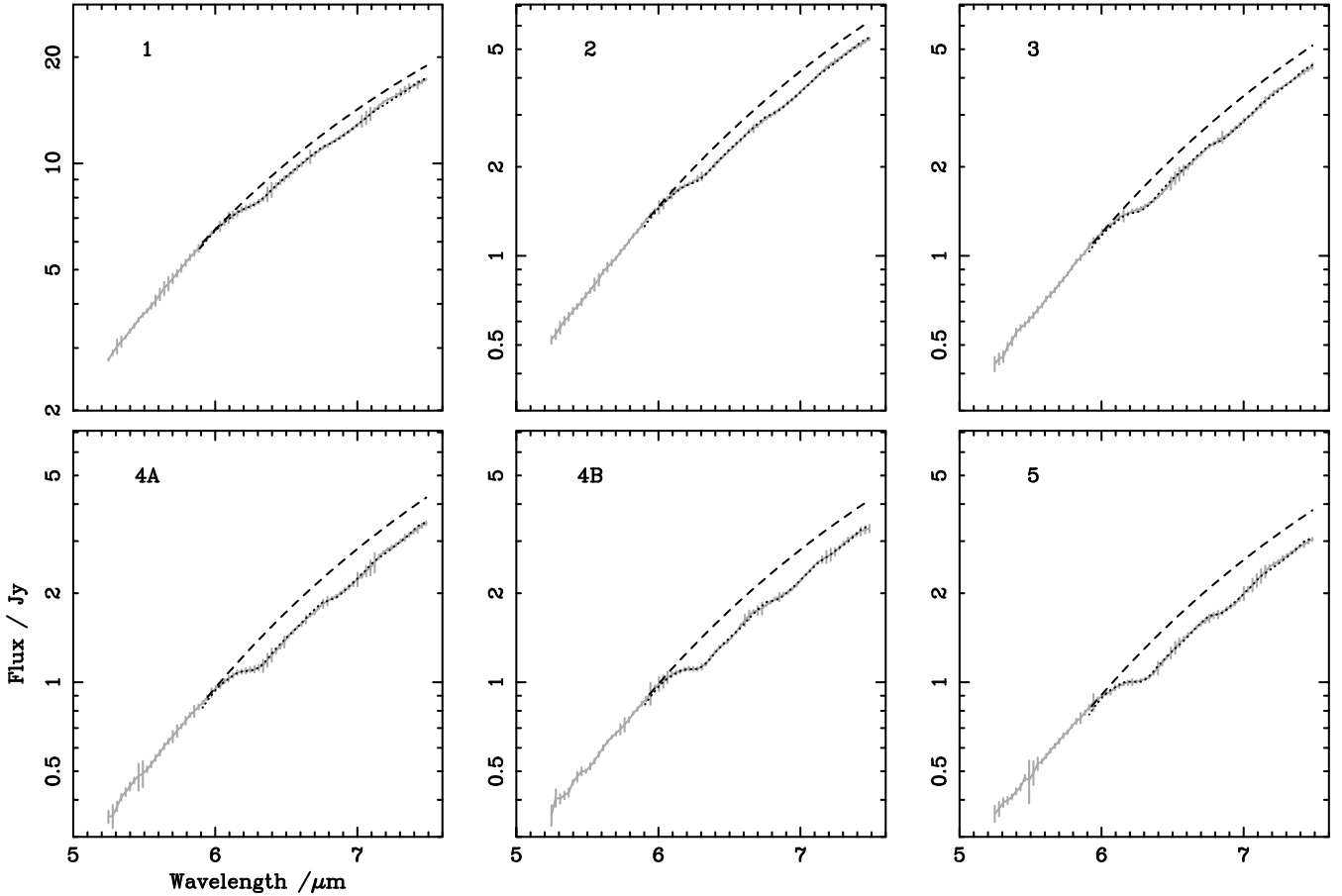


Figure 1. 5.2–7.5 μm spectra of Sakurai's object (grey error bars) with features fitted with a black body obscured by PAHs, melilite and bSiC (dotted; equation 1) and derived continua (dashed).

in the absence of water) can be ruled out as carriers of the 6.3 μm and 6.9 μm bands. However, its complex history of mass-loss and planetary nebula would suggest that carbonaceous materials, silicates and other refractory components could contribute to the absorption features.

The Spitzer observations used in this analysis are described in Section 2. Models of the 5.9–7.5 μm and 8.3–13.3 μm spectra are developed and the choice of laboratory data explained in Sections 3 and 5. The fits to each range are described in Sections 4 and 6 and the observational results summarised in Section 7. A time-averaged dust profile for the 6–7.5 μm -range is produced in Section 4.2. Dust column mass and number densities are quoted in Section 8 together with estimates of the masses of carbonaceous dust formed. The evolution of the dust during the Spitzer observations is discussed in Section 9. Conclusions are in Section 10.

2 OBSERVATIONS

Sakurai's Object was observed with the Low-Resolution Spectrometer (LRS) (Houck et al. 2004) on the Spitzer Space Telescope (Werner et al. 2004) on six occasions between 15 April 2005 and 18 October 2008 at intervals of 750, 163, 189, 9, and 171 days, respectively designated Epochs 1, 2, 3, 4A, 4B and 5 in Table 1 and Figure 2. The PI was A. Evans and the programmes were 3362, 30077 and 40061. The 5.6 μm flux fell by a factor of 4 in the between April 2005 and

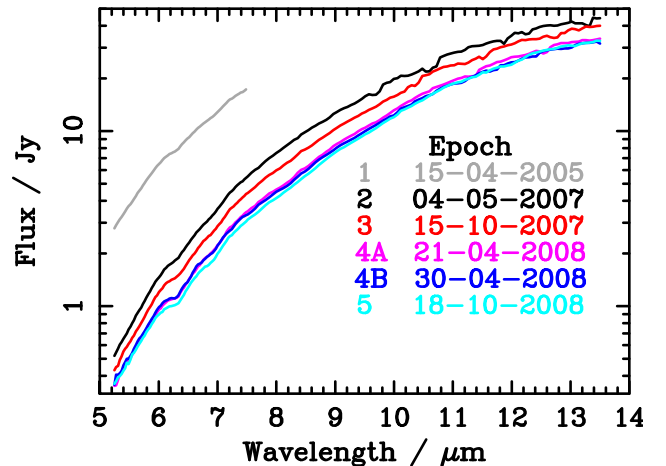


Figure 2. Merged Spitzer SL2 (5–7.5 μm), SL3 (7.5–8.5 μm) and SL1 (7.6–14.0 μm)—spectra of Sakurai's Object for Epochs 2–5. SL2 only for Epoch 1; SL1 data were saturated.

April 2007 (Epochs 1–2) and stabilised at 1/6th of the original flux between April and October 2008 (Epochs 4–5).

The Spitzer observing modes and results from both high (HR)

Table 1. Spitzer LRS Observations (Ev2020)

Epoch	MJD ^a	Date	AOR	T/K	$F_{5.6}/Jy$ ^b
1	53475	2005-04-15	10840320	284	3.54 ± 0.01
2	54225	2007-05-04	17740544	226	0.921 ± 0.003
3	54388	2007-10-15	17742336	217	0.734 ± 0.003
4A	54577	2008-04-21	17742592	–	0.591 ± 0.003
4B	54586	2008-04-30	22273280	–	0.604 ± 0.002
5	54757	2008-10-18	22272768	207	0.571 ± 0.002

^a Modified Julian Date (MJD) is used to identify the time of the observations. MJD is related to Julian Date (JD) by $MJD = JD - 2400000.5$

^b Weighted mean of 5.25–6.00 μm flux.

and low resolution (LR) observations are described by (Evans et al. 2006, AOR 10840320) and Ev2020. Pipeline-reduced and optimally-extracted spectra covering orders SL 1, 2 and 3 used in this paper were obtained from the Combined Atlas of Sources with Spitzer/IRS Spectra (CASSIS) (Lebouteiller et al. 2011) in 2020; CASSIS used data reduction pipeline S18.18.0. Fits were constrained with the combined systematic and RMS errors (the most pessimistic uncertainties); AOR 17742592 SL 1 observations were constrained only with RMS errors because this part of the CASSIS spectrum did not include systematic errors. The observations are shown with the fitted models in Figures 1 and 6(a).

Due to the disjointed nature of both the laboratory and observational data, I initially fitted 5.3–7.5 μm SL 2 spectra and then extended the analysis to the SL 1 (7.6–14.0 μm) and SL 3 (7.5–8.5 μm) bands in a piecemeal fashion. SL 1 and SL 3 spectral segments were scaled by up to ± 5 percent to match the SL 2 fluxes and the weighted means of interleaved regions obtained before fitting them. SL 1 data were trimmed at 13.5 μm before analysis to exclude a spectral artefact known as the 14- μm teardrop (see IRS 2011). HR spectra cover the the 10 μm to 37 μm range which excludes the PAH bands and half the 10 μm astronomical silicate feature modelled here. Slopes of scaled 9.9–13.5 μm HR spectra match those of the LL spectra, but the HR data are otherwise beyond the scope of this work.

3 MODEL FOR 5.9 TO 7.5 μm SL 2 SPECTRA

In order to determine the absorption optical depth profile, the likely dust components, and a continuum, the Spitzer SL 2 flux spectra were fitted with an obscured black body model with up to three foreground absorption components, where the flux, F_ν is given by:

$$F_\nu = c_0 B_\nu(T) \exp\left(-\sum_{i=1}^3 c_i \tau_i(\lambda)\right), \quad (1)$$

where $B_\nu(T)$ is the Planck function, and τ_i is the shape of the i^{th} absorption feature, normalised to unity at the tallest peak in the wavelength range of interest, and c_0 and c_1 to c_3 are the fitted scale factors. c_0 , was determined so that the continuum was matched to the feature at 6.0 μm , i.e. the foreground absorption was assumed zero at this wavelength. Absorption components were selected on the basis of their ability to the peak and width of observed absorption bands with a preference for fewer components and an improvement in χ^2 values if more components were added. Absorption components were fitted simultaneously using the down-hill simplex method of χ^2 -minimization. Laboratory data used in fitting are listed in Table 2, described in Appendices A2, and A3, and the preferred candidates

are discussed below. Optical depth profiles were obtained for each epoch by deriving a source continuum with the foreground absorption set to zero, i.e. $\tau = \ln(F_o/c_0 B_\nu(T))$, where F_o is the observed spectrum.

Due to the narrow wavelength ranges involved in fitting in comparison to the breadth of the peak of the Planck function, the black body temperature will drift to unrealistic values and other parameters will not settle if it is unconstrained. Therefore temperature was selected by trial and error to provide the lowest χ^2 . Values used were consistent with those obtained by Ev2020; where they differ significantly (Epoch 5), this is likely to be due to the $< 8 \mu m$ spectra being insensitive to the cooler dust components. The current model does not include a term for the interstellar reddening (powerlaw extinction) because, the visual extinction is low ($A_V \sim 2$; Evans et al. 2002), the photosphere obscured and the temperature relatively unconstrained. Fits to the flux spectra and continua are in Figure 1. The derived optical depth profiles of dust towards Sakurai's Object for the different Epochs and the laboratory spectra used in fitting are compared in Figure 3.

3.1 6.3 μm : Polycyclic Aromatic Hydrocarbons (PAHs)

The Hydrogenated Amorphous Carbon (HAC) compounds suggested by Ev2020, were not a good match to the features since the proposed spectra (Grishko & Duley 2002) are dominated by a broad merged 5.8 μm (attributed to carbonyl C=O) and 6.2 μm peak which is not observed in Sakurai's Object (see Appendix A1). Good eye-ball single-component matches to the $\sim 6.3 \mu m$ absorption peak and the position of the $\sim 6.9 \mu m$ peak were obtained with the spectrum of a PAH-dominated soot sample created and characterised by Carpentier et al. (2012) (see Figure 3). However, these PAH bands are too structured to match the strength and breadth of 6.9 μm absorption band without an additional component. I have not found a carbonaceous material with a sufficiently broad absorption feature at this wavelength (e.g. Gavilan et al. 2017, presented 56 spectra of PAHs in this wavelength range) and but given the complexity of dust formation this possibility cannot be completely ruled out.

3.2 Melilite as the carrier of the broad 6.9 μm band

3.2.1 Absence of ice and carbonate towards Sakurai's Object

The similar YSO and molecular-cloud 6.9- μm feature is frequently associated with methanol ice or carbonates, but neither produce an ideal match (e.g. Keane et al. 2001; Boogert et al. 2011; Bowey & Hofmeister 2005). Of these candidates methanol is preferred because its abundance in molecular clouds and YSOs is 3–30% of H₂O ice

Table 2. Laboratory data and band assignments of the C-rich (PAH, bSiC and nSiC) and O-rich (melilite and astrosilicate) dust components used in the models; mass absorption coefficients are given at the peak wavelengths marked in bold type; see the appendices for further information

Sample	Bands	Approximate Assignment	Size ^a	ρ gcm ⁻³	κ_{pk} 10 ² cm ² g ⁻¹	m_g ^b g	Ref ^c
PAH	6.3 , 6.9 7.3 8.0 11.3, 11.9	Arom. C=C stretch C–C defect Arom. CH bend	53 ⁷⁰ ₃₀ nm	0.39 ^{0.2} _{1.8}	600 ¹²⁰⁰ ₁₃₀ ^d	5.8×10^{-17}	1
bSiC	6.2, 6.6 7.1, 7.6	Overtone	25 μ m	3.2	2.4	5.0×10^{-8}	2
nSiC	12.3	Si–C stretch	3 nm	3.2	15000	8.6×10^{-20}	2, 4
melilite ^e	6.1, 6.9	Overtone	12 μ m	3.0	2.2	5.2×10^{-9}	3
astrosilicate ^f	9.8	Si–O stretch	0.3 μ m	3.3	26	8.9×10^{-14}	

^a Representative grain length assuming approximately cubic geometry.

^b Representative mass of single grain, assuming volume=(size)³

^c Reference for spectrum (also see appendices): 1–[Carpentier et al. 2012](#); 2–[Hofmeister et al. 2009](#); 3–[Bowey & Hofmeister 2005](#); 4–[Speck, Thompson, & Hofmeister 2005](#); 5–[Bowey & Adamson 2002](#)

^d Best estimates. The superscripts and subscripts indicate the range depending on the effective mass density of the soot sample, the value of 1200 pertains to a grain of 30nm and bulk mass density; see [Appendix A2](#)

^e The formula of this melilite sample is (Ca_{1.7}Na_{0.3})(Fe_{0.2}Mg_{0.4}Al_{0.4})(Al_{0.1}Si_{1.9}O₇); it is an Si-rich intermediate member of the äkermanite (Ca₂MgSiO₇) to gehlenite (Ca₂Al(AlSi)O₇) solid-solution series in which one of the Si atoms is replaced by Al.

^f Represented by the line of sight to Cyg OB2 no.12; ρ is an estimate given by the mean of forsterite and enstatite mass densities; κ_{pk} from [Bowey & Adamson \(2002\)](#).

(e.g. [Whittet 2003](#)). However, the low visual extinction and absence of a H₂O-ice detection towards Sakurai’s Object makes this identification implausible in this environment. In addition methanol ice has a narrower band, more similar to the similar to the PAH 6.9- μ m band, than to the missing absorption component. The absence of water in the environment would also preclude the existence of carbonates which form in the presence of liquid water within asteroid bodies or terrestrial environments (e.g. [Abreu & Brearley 2005](#)).

3.2.2 Oxygen-rich candidates: melilite and hibonite

Even though Sakurai is currently C-rich the presence of the old PN indicates that this may not always have been the case. Dual dust chemistries have been observed in PNe associated with Wolf-Rayet stars with PAH emission below $\sim 15\mu$ m and crystalline silicates at longer wavelengths ([Cohen et al. 2002](#)); features from both C-rich and O-rich materials are also seen in the oxygen-rich PN of NGC 6302 which displays prominent PAH emission as well as emission from crystalline silicates ([Molster et al. 2001](#)) and ([Hofmeister et al. 2004](#)) associated far-infrared emission bands with melilite and hibonite. In the near-infrared, [Bowey & Hofmeister \(2005\)](#) presented overtone spectra of ~ 30 refractory minerals present in meteorites and showed that the broad 6.9 μ m bands in YSOs are matched reasonably well by an overtone feature seen in 12 μ m-thick samples of compressed crystalline melilite powder, i.e. with an effective grain size of $\sim 12\mu$ m, or possibly $\sim 60\mu$ m-sized grains of disordered (metamict) hibonite (\sim CaAl₁₂O₁₉) (see [Appendix A3](#)). These large grains have opaque fundamental bands (e.g. Si–O stretches in melilite) and therefore undetectable at the wavelengths where astronomical mineral searches are normally conducted. Only the melilite feature is observed because melilites have particularly strong overtone features which are three times as strong those of other anhydrous crystalline silicates

(e.g. forsterite, pyroxenes, feldspars) and ten times those of forsterite and diopside glass (see [Bowey & Hofmeister 2005](#)).

Melilites are an important component of calcium-aluminium-rich inclusions (CAIs) in primitive meteorites. CAIs are early high-temperature condensates in solar nebular theories (e.g. review by [Rubin & Ma 2017](#)). CAI abundance in the most primitive (CO3) chondrites is ~ 1.5 area per cent¹ with an average CAI size of $98.4 \pm 54.4\ \mu$ m ([Zhang et al. 2020](#)). Melilite-rich inclusions and spinel-pyroxene CAIs comprise 80-100 percent of the total CAIs for each chondrite; [Zhang et al.](#) argued that the spinel-pyroxene CAIs in these and more processed meteorites are alteration products derived from melilites and found that a subset of fluffy melilites were composed of loosely aggregated $< 15\mu$ m-sized melilite grains.

Hibonite is less plausible because the fits are poorer, fewer than 4.8 per cent of CAIs in meteorites are hibonite (and grossite; \sim CaAl₄O₇)-bearing ([Zhang et al. 2020](#)), with the metamict form being relatively rare and other hibonites have weaker overtones which do not occur at 6.9 μ m, and hibonite bands are bands are 5-30 times weaker than the melilite feature (see [Appendix A3](#) and [Bowey & Hofmeister 2005](#)).

Since Sakurai’s Object has had a complicated history of mass-loss and is surrounded by a PN and an interstellar silicate absorption feature was detected by [Evans et al. \(2002\)](#) and no other candidate has been found I modelled the data with a melilite component ([Figure 3](#)). Statistics of two component fits ($\chi^2_{\nu 2}$) are given in [Table 3](#) and the sum of the PAH and melilite components of the fit to Epoch 5 indicated by the dashed curve in [Figure 3](#).

¹ i.e. on average 1.5 per cent of the surface area of the sampled meteorite slices were comprised of CAIs; this number is very similar to the volume per cent. Some other chondrite types, especially CVs have more, with ~ 3 area per cent on average (e.g. [Hezel et al. 2008](#)).

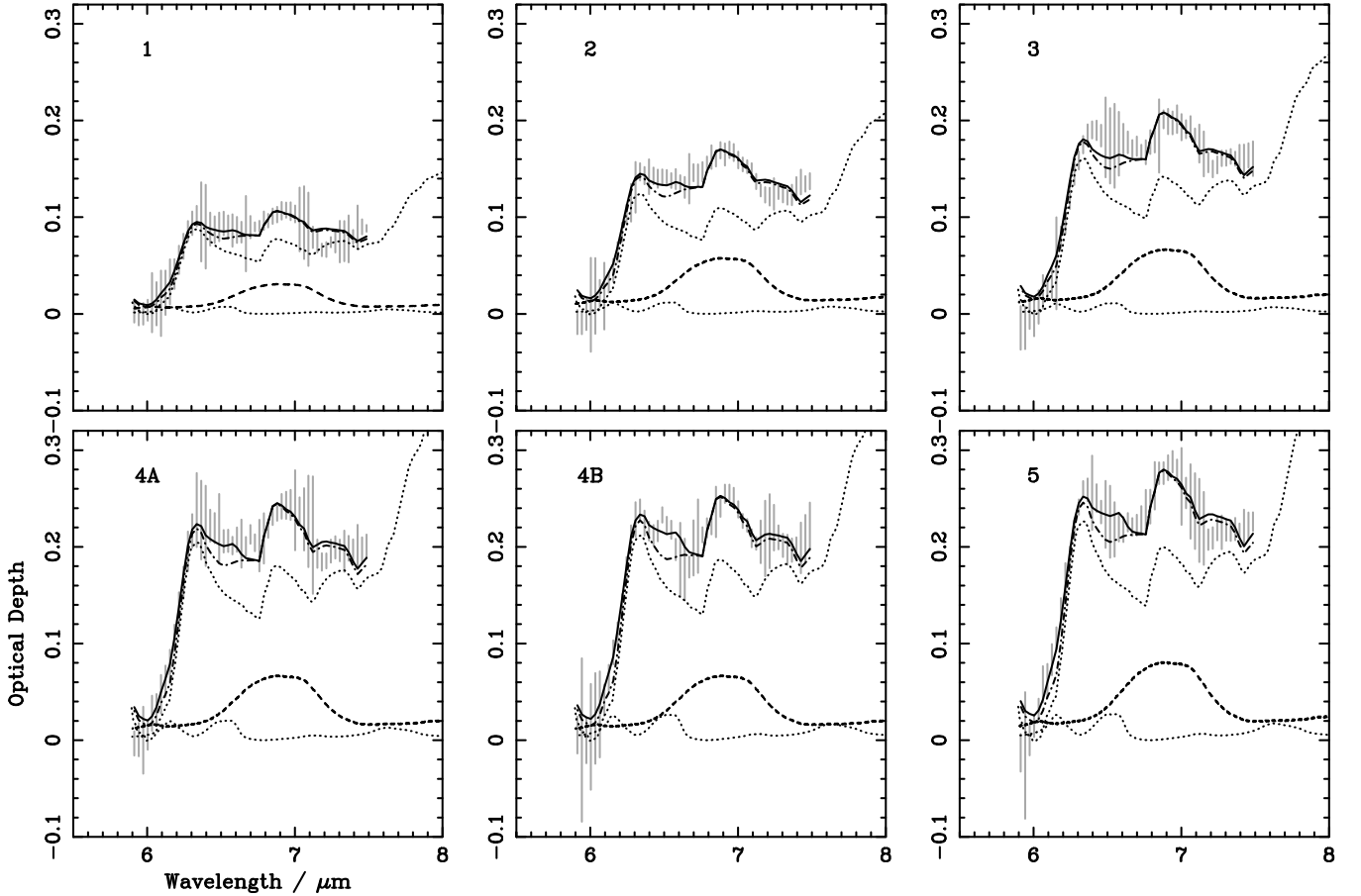


Figure 3. 6–7.5 μm optical depth profiles of Sakurai's Object (error bars) with fits (solid); fitted PAH (dotted -top), bSiC (dotted) and melilite (dashed) components. Dot-dash curves indicate the effect of removing the bSiC component from the fits.

3.3 A component due to 25 μm -sized Carbide Grains?

Isotope measurements exist for thousands of 0.1–20 μm -sized meteoritic grains with non-solar isotope ratios of pre-solar origin (e.g. Hoppe et al. 1994; Speck, Thompson, & Hofmeister 2005) suggesting that they somehow travelled from C-stars to the Solar Nebula. However, SiC has not been detected in the interstellar medium (e.g. Whittet, Duley, & Martin 1990). This is probably a consequence of its high opacity, since grains have to be nanometre-sized to produce reliable unsaturated bands (see Hofmeister et al. 2009). However, $\lesssim 25 \mu\text{m}$ SiC grains, hereinafter denoted bSiC (for “big” SiC grains), produce small peaks at 6.2 and 6.6 μm , whilst being opaque in their fundamental Si-C stretch at 12.3 μm (Hofmeister et al. 2009, see Appendix A3 for its derivation), so I included them in three-component models. Due to slight rounding of the 6.6 μm peak, 25 μm is likely to be an upper size limit (see Appendix A3).

4 5.9 – 7.5 μm FITS

The best three-component fits to each Epoch are listed in Table 3 and plotted with the observations and continua in Figure 1. Derived optical depth profiles are plotted with the modelled laboratory components in Figure 3. The increases in c_{pah} , c_{mel} and c_{SiC} with time will be discussed in Section 4.1.

At Epochs 1 and 3 the observational uncertainties are too large giving confidence intervals > 50 percent and little improvement in

χ^2_v with three components and the SiC contribution is quoted as an upper limit. Fits to Epochs 2, 4A, 4B and 5 were slightly better with a bSiC component (improvement in χ^2_v 0.05–0.33) and the 1-sigma confidence intervals for bSiC were $\sigma_{bSiC} < 30$ per cent, with little change in c_{pah} (0–10 per cent lower) and c_{mel} (increased by 7–10 per cent) for all but Epoch 5, where c_{pah} and c_{mel} decreased by 50 per cent and 4 per cent, respectively. The improvement in fit quality was due to the 6.2 and 6.6 μm bands combining with the 6.3- μm PAH band to broaden it and flatten the interval between it and the 6.9 μm band (compare solid and dot-dash curves in Figure 3). The modelled bSiC components will be extrapolated in Section 6.4 to show the influence of weaker 7.1 and 7.6 μm overtones.

4.1 Increases in PAH, melilite and bSiC with time

The fitted PAH, melilite and bSiC optical depths at each Epoch are listed in Table 3 and plotted against their modified julian dates (MJD; Table 1) Figure 4. In the Figure each parameter has been ratioed to its value at the earliest Epoch, MJD₀, with a proper detection (not an upper limit). Hence, c_{pah} and c_{mel} are ratioed to values at Epoch 1, whilst c_{SiC} is ratioed at Epoch 2.

Slopes of linear fits to c_{pah} and c_{mel} indicate increase rates of $0.44 \pm 0.01 \text{ yr}^{-1}$ and $0.40 \pm 0.04 \text{ yr}^{-1}$. These rates are consistent with Ev2020's $0.6 \pm 0.2 \text{ yr}^{-1}$ estimate of the rate of increase in dust mass from the emitted flux (λF_λ) within the uncertainties, even though the absorbing grains may have been formed at an earlier time. Within the

Table 3. Fits to 5.9–7.5 μm spectra of Sakurai’s object: black body absorbed by PAHs, melilite, and bSiC. The 1 sigma confidence intervals σ , for c_{pah} are 1–2 per cent; for c_{mel} they are normally 4–5 per cent and 7 per cent in Epoch 1. $\tau_{6.3}$ and $\tau_{6.9}$ are the measured optical depths of the 6.3 and 6.9 μm peaks, respectively. χ^2_ν and $\chi^2_{\nu 2}$ denote three-component and two-component (PAH and melilite only) fits, respectively.

Ep.	T/K	c_{pah}	c_{mel}	c_{SiC}	σ	χ^2_ν	$\chi^2_{\nu 2}$	$\tau_{6.3}$	$\tau_{6.9}$
1	275	0.085	0.031	<0.007	59	0.90	0.91	0.10	0.11
2	226	0.13	0.058	0.011	28	0.96	1.1	0.15	0.17
3	224	0.16	0.067	<0.010	50	0.99	1.0	0.19	0.20
4A	222	0.20	0.067	0.020	26	0.77	0.91	0.23	0.24
4B	227	0.21	0.067	0.026	15	0.52	0.85	0.24	0.26
5	227	0.23	0.081	0.027	20	0.70	1.0	0.26	0.28
WM		0.80	0.29	0.098		4.3		0.90	1.0

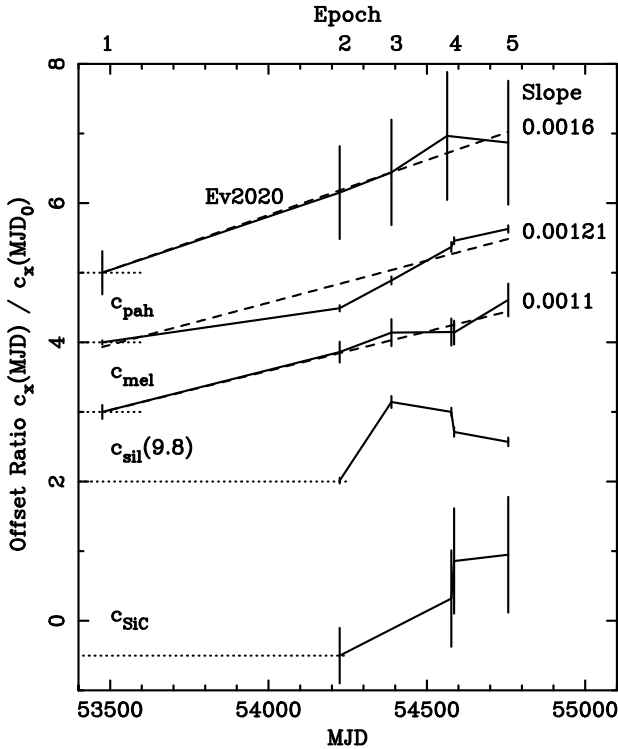


Figure 4. Increases in dust mass during the Spitzer observing period. Values obtained by *Ev2020* are from the flux method. c_{pah} , c_{mel} and c_{SiC} are the fitted optical depths of the small PAH and melilite and bSiC overtones, respectively. Each indicator, except c_{SiC} , is ratioed to the value at Epoch 1 (2005-04); c_{SiC} is ratioed its value at Epoch 2 (2007-05). Offsets are indicated by dotted lines. Slopes in the figure are in optical depth per day, Uncertainties in the fitted slopes are 0.0005 (?), 0.00004 (c_{pah}), 0.0001 (c_{mel}) per day.

1-sigma confidence intervals, the slope of c_{pah} appears to increase to $0.99 \pm 0.06 \text{ yr}^{-1}$ during Epochs 2–4B before readopting the slower rate of increase between Epochs 4B and 5. c_{mel} increases between Epochs 1 and 5. There is an apparent increase in bSiC with a jump between 4A and 4B but the uncertainty in this is large.

4.2 Weighted mean optical depth profile

Since variation in the relative proportions of the dust components is small it is possible to obtain a higher signal-to-noise time-averaged

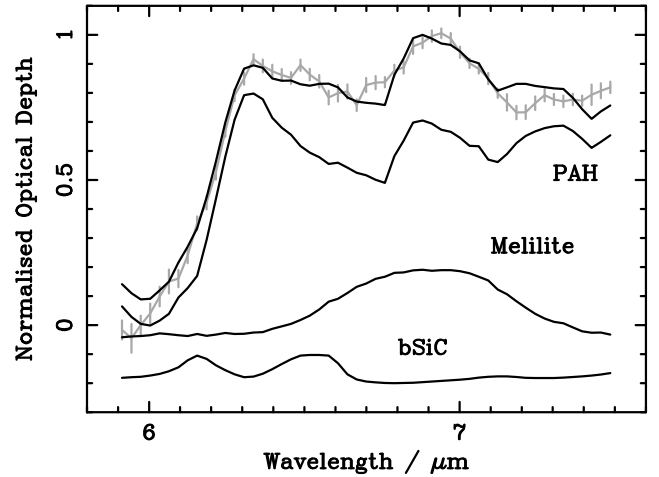


Figure 5. Weighted mean of normalised optical depths (grey) with 3 component fit (black) and components below.

6–7 μm dust profile for comparison with dust features other environments such as molecular clouds and YSOs. The profile was obtained after normalising the profiles from Epochs 1 to 5 at 6.9 μm . The weighted mean dust profile, together with fits of the PAH, melilite and bSiC components, is presented in Figure 5. As expected, fits to the PAH, melilite and bSiC features resemble those of the strongest features observed in Epoch 5; when scaled to $\tau_{6.9}$ they are, 0.22, 0.81, 0.027, respectively: only c_{pah} is slightly lower, reflecting its faster growth rate.

5 FITTING 8.4–13.3 μm SPECTRA

Longer-wavelength observations at Epochs 3 and 4A appeared to have a narrow absorption feature at 11.3 μm (Figure 6(a)) so a single-component PAH model was extended to derive a continuum for it. Melilite and bSiC components were not included because these grains are opaque in this wavelength range. However, fits with Equation 1 did not match the overall shape of the flux spectrum until a foreground ‘interstellar’ 10 μm silicate absorption feature was added, represented by the diffuse-medium dust profile towards Cyg OB2 no. 12, hereinafter called astrosilicate; the feature shape, shown in Figure 9(b) $\tau_{sil}(\lambda)$ is derived in Appendix A4.

Fits were further improved when a single-temperature optically-thin emission component due to nanometer-sized SiC grains, called

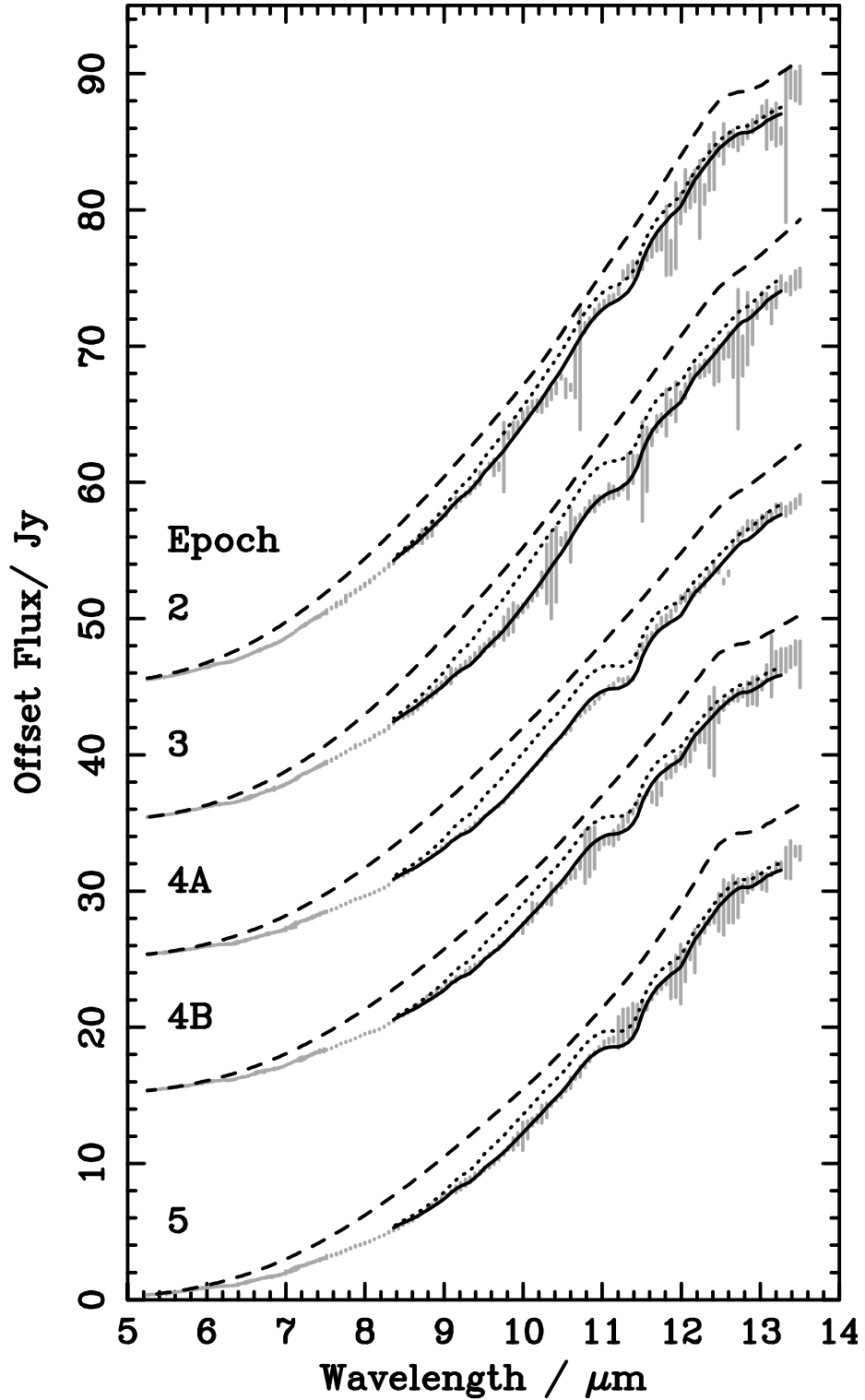


Figure 6. Fits between 8.3 and 13.3 μm . (a) 8.3 and 13.3 μm fits (solid curves) to the SL1 flux spectra (grey error bars) using the PAH fit to the SL 2 data; dotted curves – effect of removing foreground silicate absorption; dashed curves - modelled continua when the foreground absorption is zero. Y-axis offsets (bottom to top) are 0.0, 15, 25, 35 and 45 Jy.

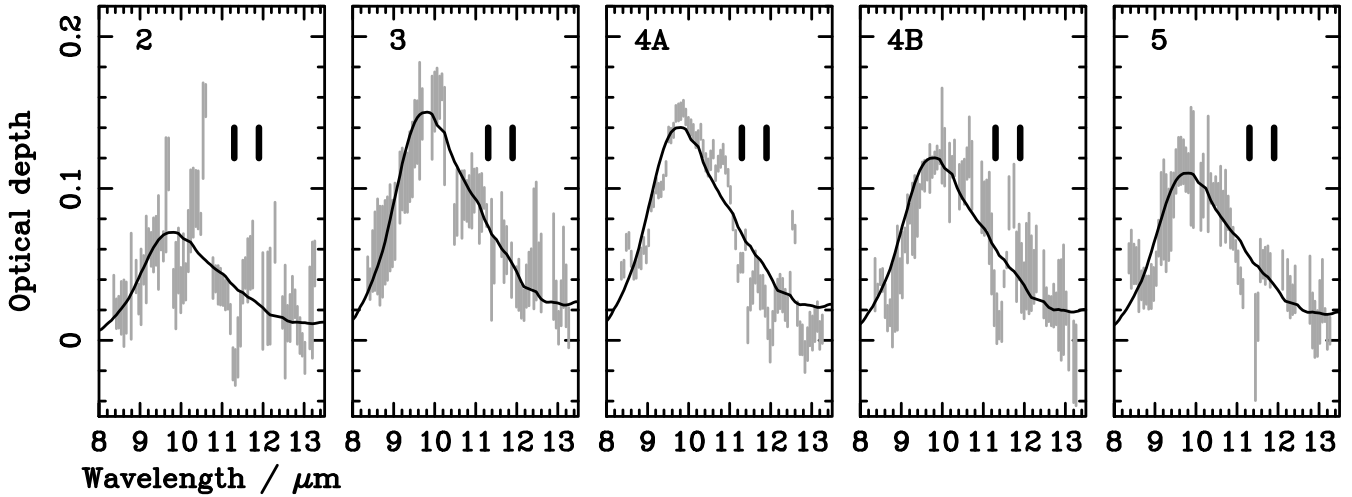


Figure 7. Changes in the 10- μm astrosilicate absorption compared with Cyg OB2 no. 12 after subtraction of the PAH component. Noisy points (uncertainty > 0.04) have been removed for clarity. Bars indicate the centres of PAH bands, which may be too deep.

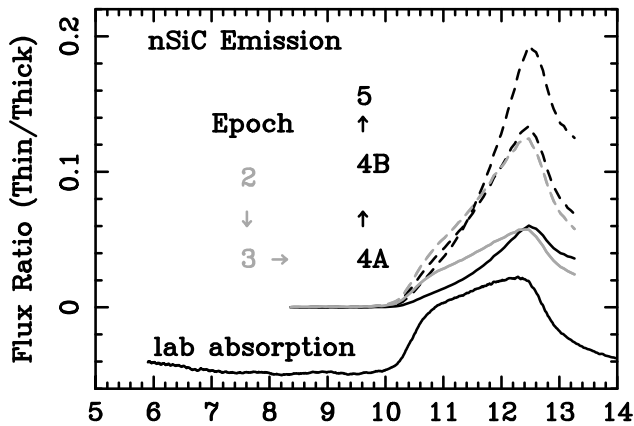


Figure 8. Modelled nSiC emission: when the 11.3- μm PAH absorption band matches the observations (solid), dashed when it does not. Grey and black curves indicate falling and rising optically-thin fractions, respectively. The laboratory profile of nSiC is shown below (arbitrary normalisation; offset -0.05 in the Y-axis).

nSiC (see Figure 8), was added so that the source flux, F_{ν^*} is given by,

$$F_{\nu^*} \propto B_{\nu}(T_1) + B_{\nu}(T_2)c_{nSiC}\tau_{nSiC}(\lambda) \quad (2)$$

where T_1 and T_2 are the temperatures of the optically-thick and optically-thin emission components and c_{nSiC} is a scaling constant for normalised nSiC emission, $\tau_{nSiC}(\lambda)$. This emitted continuum was then extinguished by foreground astrosilicate dust to give the observed flux, F_{ν} ,

$$F_{\nu} = c'_0 F_{\nu^*} \exp(-c_{pah}\tau_{pah}(\lambda) - c_{sil}\tau_{sil}(\lambda)) \quad (3)$$

where, scaling constant c'_0 , T_2 and c_{sil} were fitted by χ^2 -minimization and c_{pah} was fixed to the value obtained from the 5.9–7.5 μm fits. Continua for merged SL 1–SL 3 5–13.5 μm spectra were derived by setting c_{pah} and c_{sil} , to zero and extending the wavelength range.

5.1 Constraints and exclusions

No attempt was made to model the 7.5–8.3 μm -range for several reasons: (i) there are inherent uncertainties in the LRS observations because of merging between orders, (ii) laboratory spectra of PAHs show a great deal of variability in the shape of the defect band, (iii) silicate overtones merge with Si–O bands making results highly dependent on the baseline subtraction in the laboratory data (see [Bowey & Hofmeister 2005](#)), (iv) the bSiC and melilite grains responsible for overtone features are a separate population to the submicron-sized and nanometer-sized grains responsible for features between 8–13 μm and it is not clear how to merge the data in these simple models.

Since the PAH bands surround the 10- μm silicate absorption band (Figure 9(b)) c_{pah} was set to zero to explore the interplay between them. In these cases statistically better fits were obtained, the temperature was ~ 20 -K cooler, optically-thin emission negligible and the foreground silicate absorption very weak. These fits were disregarded because the fluxes of these continua fell well-below the fluxes of the merged 5–8 μm spectra which is inconsistent with a central stellar energy source.

6 8.3–13.3 μm FITS

The observations (grey error bars), fits (solid curves) and continua (dashed curves) are displayed in Figure 6. If the silicate absorption component is excluded the fits do not match the curvature of the observations between 11 and 12 μm (dotted curves). Fitted parameters are listed in Table 4. 11.3 μm absorption bands in Epochs 3 and 4A are well-matched by the modelled SL 1 PAH strengths, but the absorption bands are not observed at other Epochs. Epoch 2 might have a narrow PAH emission band at 11.3 μm , but this may be coincidental with the noise.

Fits to all Epochs required both optically-thick and optically-thin emission components and the proportion of optically-thin nSiC emission varied with time. The temperature of the optically-thick component was usually 1–3-K warmer than the 6–7 μm continuum, but Epoch 2 required a 11 K higher blackbody temperature and weaker

Table 4. Fits to 8–13 μm SL 1 spectra of Sakurai's Object, T_1 (pre-set) and T_2 (fitted) are the temperatures of the optically-thick and optically-thin components, respectively. Sakurai was not observed at 8–13 μm during Epoch 1.

Epoch	T_1 K	T_2 K	$\epsilon_{12.5}$	$F_{12.5}^a$ Jy	$c_{sil}(\sigma^b)$	χ^2_ν	PAH? 11.3
2	237	119	0.123	40.3	0.071 (3)	3.5	–
3	225	137	0.057	33.8	0.15 (2)	0.77	Y
4A	225	81	0.059	28.7	0.14 (0.7)	8.4 ^c	Y
4B	228	100	0.132	28.5	0.12 (2)	1.8	–
5	228	75	0.191	28.0	0.11 (2)	1.2	–

^a Weighted mean flux between 12.0 and 13.0 μm ; ± 0.1 Jy plus order match uncertainty

^b 1 sigma confidence interval per cent.

^c Reflects only RMS errors; CASSIS did not output systematic errors for SL 1

foreground silicate absorption ($\tau \sim 0.07$); the difference is caused by narrow-band structures in the spectrum of unknown origin at 9.7 and 10.5 μm – either unidentified gas-phase absorption or noise since the error bars are large. The temperature of the optically-thin component, T_2 , settled on values 50–155 K cooler than the optically-thick emission but the absence of an identifiable trend indicates it is not well-constrained.

6.1 Temporal variation in the 10 μm astrosilicate absorption

Fitted optical depths of the foreground silicate absorption, c_{sil} , are within ± 0.04 of the 0.105 ± 0.005 value deduced by Evans et al. (2002) and modelled values increase between Epochs 2 and 3 before decreasing between Epochs 3 and 5 (Figure 4 and Table 4). The silicate absorption profiles are shown in Figure 7 after subtraction of the modelled PAH absorption: the feature in Epoch 2 is not really detected above the noise but changes in the features between Epochs 3 and 5 are significant and inconsistent with a homogeneous distribution of *interstellar* silicate along the line of sight which is unrelated to Sakurai's Object. It is plausible that some of the astrosilicate absorption is due to dust distributed within the ancient PN and that disturbances associated with the eruptive dust-formation event are causing silicates to coagulate into larger grains. The interstellar feature towards Cyg OB2 no. 12 dust can still be used for modelling because the profile is similar in shape to the emission from new dust surrounding the O-rich AGB star μ Cephei (e.g. Bowey, Rawlings, & Adamson 2004). The relationship between the decrease in astrosilicate and possible increase in melilite in Epoch 5 will be explored in Section 9.2

6.2 Temporal variation of optically-thin nSiC emission

The ratios of the optically-thin emission to the optically-thick emission at each Epoch are compared in Figure 8. The optically-thin component is smallest at Epochs 3 and 4A, in which the 11.3- μm absorption feature matches the 6–7- μm fits. The fraction of optically-thin emission is largest when the fitted silicate absorption is weakest indicating that during fitting the two parameters work together to increase the curvature of the flux spectrum to make it rise at longer wavelengths.

Both the the total flux and the proportion of optically-thin emission decreased between Epochs 2 and 3. Between Epochs 3 and 4A the

flux decreased more slowly and the optically-thin component did not change significantly (though it might have cooled). The flux did not change between Epochs 4A and 5, but became significantly more optically-thin, changing rapidly in the in the 9 days between Epochs 4A and 4B (April 2008). Unfortunately it is impossible to know if the apparent increase in the optically-thin component in the 171 days between Epochs 4B and 5 occurred as rapidly as the change in the days preceeding it.

6.3 5.9–13.3 μm Absorption Components

Optical depth profiles for Epochs 2–5 are compared with absorption profiles fitted to the 8.3–13.3 μm and 6–7.5 μm data (solid curves) in Figure 9(a); short dotted curves show an extrapolation of the bSiC contribution (Section 3.3). Offsets are added to the 6–7.5 μm fits to allow for the difference in scaling constants c_0 and c'_0 . The discrepancy between the slopes of the 6–7.5 μm fit and the profile for Epoch 2 is caused by the 11 K difference in the temperature of the optically-thick emission.

6.4 PAH and bSiC

The 11.3- μm PAH absorption features in Epochs 3 and 4A match the band strengths implied by 6–7.5 μm values of c_{pah} . However, the observed 11.3 μm PAH absorption is negligible in Epochs 4B and 5. The feature might occur in emission at Epoch 2. It is conceivable that the observed changes are consistent with the trend in nSiC emission because as time progresses the PAH feature moves from emission, to absorption followed by the emission feature filling in the absorption feature - but there is insufficient data to prove this.

There is also some correlation between the shape of excess absorption near 8.0 μm and the shape and position of the C=C defect band (Figure 9(b)) even though this is probably suppressed by unconsidered emission or absorption components in the line of sight. Surprisingly, the extrapolated weak bSiC features identified in the 6–7.5 μm data resemble the shape of weak structure in the merged spectra between 7.2 and 8.0 μm but the uncertainties are large. If the features are real, the 6.0– 8.0- μm spectral region is the place to reconcile astronomical and meteoritic studies of SiC grains. The existence of warmer nSiC grains and cool bSiC grains is consistent with Speck, Thompson, & Hofmeister (2005)'s hypothesis that SiC grains become smaller as the star evolves.

7 SUMMARY OF OBSERVATIONAL RESULTS

During the period of the Spitzer observations:

- (i) The mid-infrared flux decreased. The 5.6 and 12.5 μm fluxes decreased rapidly between Epochs 1 and 2, but the rate of change slowed between Epochs 2–4A and stopped between Epochs 4A and 5.
- (ii) The proportion of optically-thin emission decreased between Epochs 2 and 3, did not vary between Epochs 3 and 4A (though it might have become cooler) before increasing rapidly in the 9 days between Epochs 4A and 4B and increasing more slowly into Epoch 5.
- (iii) The mass of cold carbonaceous dust increased. PAH absorption increased throughout the observations, possibly with the rate accelerating during Epochs 2–4B, and then slowing between Epochs 4B and 5. Concurrent increases in bSiC abundance might be significant, but are particularly affected by the low sensitivity to the overtone features at Epochs 1–3.

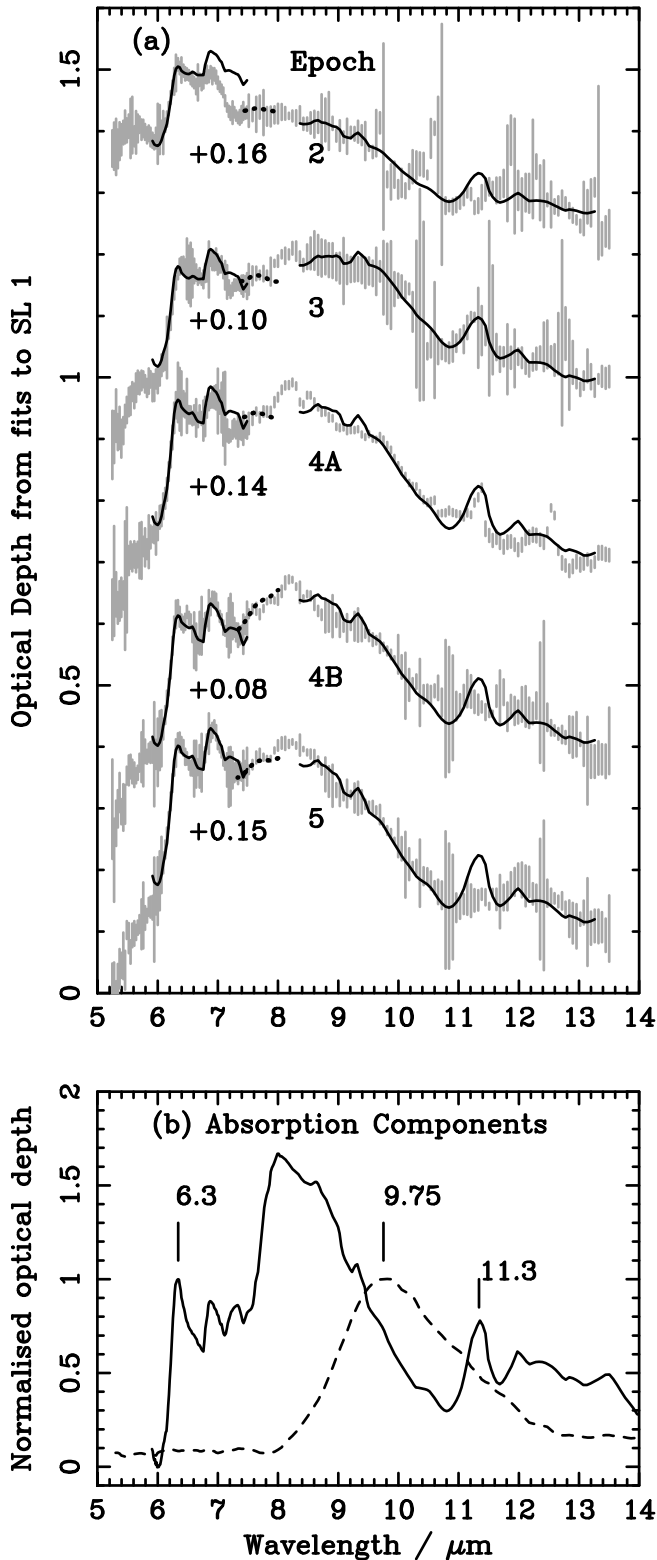


Figure 9. (a) Optical depth profiles (grey error bars) obtained with modelled 8.3–13.3 μm continua; offsets in the Y-axis are 0.0, 0.3, 0.6, 0.9 and 1.2; 8–13 μm black solid curves are the fitted absorption features, 6–7.5 μm are the fitted features from the SL 2 offset in the Y-axis to match the level of the longer-wavelength fits (additional offsets are indicated); dotted curves between 7.5 and 8.0 μm indicate the contribution from bSiC extrapolated from the SL 2 fits. (b) Absorption profiles used to model 8.3–13.3 μm spectra: PAH spectrum (solid) and silicate absorption (dashed) modelled with the profile of interstellar dust towards Cyg OB2 no. 12. Profiles are normalised at 6.3 and 9.75 μm , respectively.

(iv) The apparent composition of the cold oxygen-rich dust changed with more melilite and less astrosilicate. The melilite absorption increased between Epochs 1 and 5. The astrosilicate abundance decreased between Epochs 3 and 5.

Some of the spectral changes are subtle and their significance affected by observational sensitivities. I believe changes in the features to be real because they progressed between multiple observations and some features were modelled independently in different spectral ranges.

8 ESTIMATES OF MASS COLUMN DENSITY, NUMBER DENSITY AND DUST MASS

8.1 Mass Column Density and Number Density

An estimate of the mass column density of dust surrounding the region of optically-thick emission can be obtained because the peak optical depth, τ_{pk} , of an absorber is related to the mass absorption coefficient, κ_{pk} :

$$\tau_{pk} = \rho \kappa_{pk} L, \quad (4)$$

where ρ is the effective mass density of the absorber and L is the path-length of the light through the dust so that the mass column density of absorbers, Σ along the line of sight is given by:

$$\Sigma = \rho L = \tau_{pk} / \kappa_{pk}. \quad (5)$$

The column number density of grains is obtained by dividing Σ , by the single-grain masses, m_g , in Table 2. The mass and grain column densities are listed in Table 5.

8.2 Rates of increase in Mass Density and Number Density

Equation 5 and the rates of change of PAH and melilite optical-depths obtained in Section 4.1 can be used to deduce the rate of increase in mass and number density: the average rate of increase in PAH density between Epochs 1–5 is $d\Sigma_{pah}/dt = 7.3 \times 10^{-6} \text{ gcm}^{-2}\text{yr}^{-1}$ ($1.3 \times 10^{11} \text{ grains cm}^{-2}\text{yr}^{-1}$) and the enhanced rate between Epochs 2 and 4B is $d\Sigma_{pah}/dt = 17 \times 10^{-6}$ ($2.8 \times 10^{11} \text{ grains cm}^{-2}\text{yr}^{-1}$). For melilite, the mean rate of mass density increase, $d\Sigma_{mel}/dt = 1.8 \times 10^{-3} \text{ gcm}^{-2}\text{yr}^{-1}$ or $0.35 \times 10^6 \text{ grains cm}^{-2}\text{yr}^{-1}$.

8.3 Dust Mass estimates and their rate of increase

Since mass column density is related to the effective mass density of a dust grain, Equation 4 can be used to estimate the total dust mass of each component at each Epoch with the caveats that neither the distance to Sakurai’s object, nor the geometry of the dusty region associated with it, nor the mass absorption coefficient of PAHs are well-defined (see Appendix A2 for my derivation of κ_{pk}). Estimates of the distance to Sakurai’s Object vary considerably (reviewed by [Hinkle & Joyce 2014](#)). I adopt a distance of 3.5kpc which is the maximum used by [Chesneau et al. \(2009\)](#) in models of their mid-infrared observations and consistent with [Ev2020](#)’s preferred value of $3.8 \pm 0.6 \text{ kpc}$. [Chesneau et al. \(2009\)](#) obtained mid-infrared interferometer observations of Sakurai’s object on 2007 June 29–30 (MJD 54280–54281; 55 days after Epoch 2) and deduced that the source is surrounded by an opaque dusty torus or thick disk of $105 \times 140 \text{ AU}$ and a scale height of $47 \pm 7 \text{ AU}$.

Assuming that the cold PAHs and bSiC grains are located in the torus I use a cylindrical geometry to give a volume of πR^3 , where

Table 5. Column Mass Density and Number Density for Carbonaceous and Oxygen-rich dust Components

Grain Size Dust	Carbonaceous Dust						Oxygen-rich Dust			
	Mass Density		nSiC	Number Density			Mass Density		Number Density	
	PAH	bSiC $10^{-6} \text{ g cm}^{-2}$		53 nm	25 μm	3 nm	melilite $\times 10^{-6} \text{ g cm}^{-2}$	astrosilicate	12 μm	< 0.3 μm cm^{-2}
Epoch										
1	1.4 ^{6.5} _{0.71}	–	–	2.4 $\times 10^{10}$	–	–	140	–	27000	–
2	2.2 ¹⁰ _{1.1}	46	0.082	3.8 $\times 10^{10}$	920	9.5 $\times 10^{11}$	260	27	50000	3.0 $\times 10^8$
3	2.7 ¹² _{1.3}	–	0.038	4.7 $\times 10^{10}$	–	4.4 $\times 10^{11}$	310	58	60000	6.5 $\times 10^8$
4A	3.3 ¹⁵ _{1.7}	83	0.039	5.7 $\times 10^{10}$	1660	4.5 $\times 10^{11}$	310	54	60000	6.1 $\times 10^8$
4B	3.5 ¹⁶ _{1.7}	110	0.088	6.0 $\times 10^{10}$	2200	10 $\times 10^{11}$	310	46	60000	5.2 $\times 10^8$
5	3.7 ¹⁷ _{1.8}	113	0.13	6.4 $\times 10^{10}$	2300	15 $\times 10^{11}$	370	42	71000	4.7 $\times 10^8$
WM ^a	3.3 ¹⁵ _{1.7}	100	0.073	5.7 $\times 10^{10}$	2000	8.4 $\times 10^{11}$	330	50	68000	5.6 $\times 10^8$

^a PAH, bSiC and melilite -from fits to weighted mean spectrum scaled to mean of Epochs 3–5 ($\tau_{6.9} = 0.25$); nSiC and astrosilicate from mean of Epochs 3–5.

R is 50 AU and the optical path length from the optically-thick shell $L = R$ so that the mass, M , of dust in the torus due to an absorber is approximated by

$$M = \Sigma \pi R^2 \quad (6)$$

$$M_{50\text{AU}} \approx 8.8 \times 10^{-4} \Sigma M_{\odot} \quad (7)$$

and the rate of mass increase can be deduced by replacing Σ with $d\Sigma/dt$. An inferred mass of nSiC is not given because the optically-thin emission probably derives from a region closer to the optically-thick ‘photosphere’ of unknown volume.

For the 50AU torus, $d\Sigma_{\text{pah}}/dt$ equate to an average mass increase of $6.4 \times 10^{-9} M_{\odot} \text{ yr}^{-1}$ and an accelerated rate between Epochs 2 and 4B of $16 \times 10^{-9} M_{\odot} \text{ yr}^{-1}$; the faster rate is similar to [Evans et al. \(2020\)](#) estimate in May 1999, which was $11 \times 10^{-9} M_{\odot} \text{ yr}^{-1}$, when scaled to the PAH density, but lower than the rate of $40 \times 10^{-9} M_{\odot} \text{ yr}^{-1}$ in Sept 2001.

9 EVOLUTION OF THE DUST

9.1 PAH, bSiC and nSiC

My dust mass estimates are compared with [Ev2020](#) masses deduced from optically-thick emission in Table 6. [Ev2020](#) estimates have been scaled to PAH and SiC mass densities, as appropriate, and a distance of 3.5 kpc. Since it is impossible to distinguish between dust types in their data, I have converted their values for amorphous carbon to PAH and SiC masses and quoted both for blackbody temperatures between the PAH condensation temperature of 850 K ([Helling et al. 1996](#)) and 650 K. I assume that the bulk of their 200–300 K dust is formed of PAHs. The black-body temperature of 1210 K on 18 August 1998 (MJD 51043; [Geballe et al. \(2002\)](#)) was low enough for SiC condensation, but too hot for PAH formation so I assume that this is SiC dust. It is plausible that the inferred absorbing 20 μm bSiC grains were formed at this stage followed by the nanometre-sized grains in the modelled optically-thin emission. This interpretation

is consistent with [Speck, Thompson, & Hofmeister’s](#) observational and laboratory-based hypothesis that SiC grains in AGB stars grow to large sizes in early condensation phases when the mass-loss rate is low but that they become nm-sized when the stellar mass-loss rate increases.

My inferred masses of bSiC and PAHs for Epochs 1–5 are, respectively, 2 and 3 orders of magnitude lower than [Ev2020](#) estimates from the optically-thick emission on the same dates but our methods measure different grain populations: [Ev2020](#) measurement of optically-thick emission infers the dust mass of the coolest external edge of the expanding shell². My method estimates the mass of absorbing dust in front of the optically-thick region. This dust is not emitting at 6–7 μm so it must be cooler; I agree, with [Ev2020](#), that this cooler dust must be older than dust in the optically-thick shell.

PAH formation probably occurred from around 21 April 1999 (MJD 51289) when the temperature was 841 K and the SiC dust mass was $32 \times 10^{-9} M_{\odot}$, a value similar to the $41 \times 10^{-9} M_{\odot}$ estimate of mass in large SiC grains in Spitzer Epoch 2 (4 May 2007). The effect of this rapid condensation is seen in [Ev2020’s](#) third measurement on 3 May 1999 (MJD 51301) in which there is a nearly four-fold increase in mass and the temperature has dropped by 100 K in the 12 days following the previous measurement followed by little change both values in measurements 36 and 42 days later (08 and 14 June 1999).

The increases in the 6–7 μm PAH absorption seem to record this condensation event in the enhanced rate of change in the 6.3 μm PAH absorption between Epochs 2 and 4B and the reduced rate to Epoch 5. The cold dust masses observed in the Spitzer data during

² The mass estimate is sensitive to increases in surface area, but insensitive to warmer conditions inside the shell where most of the condensation occurs. Therefore foreground cool dust includes SiC dust condensed at an early time, but this contributes a decreasing fraction of the total mass. Due to the increasing surface area of the expanding dust shell and the low temperature of the optically thick leading edge inferred dust masses at the 200–300 K temperatures will probably reflect some geometric effects but an effect of 2–3 magnitudes seems unfeasibly large.

Table 6. Estimated masses of carbonaceous dust (PAH and bSiC) in the 50 AU torus compared with [Ev2020](#) estimates by the peak flux (λF_λ) method after conversion to PAH or SiC mass densities instead of amorphous carbon ($\rho = 1.5\text{gcm}^{-3}$) and scaled by 0.85 to reflect the choice of $D=3.5$ kpc.

Ep.	Date ^a	6–7 μm mass		λF_λ	λF_λ mass similar to 6–7 μm mass			
		PAH	bSiC	PAH	Date	PAH	SiC	T
		$10^{-9} M_\odot$				$10^{-9} M_\odot$		K
1	15-04-2005	1.2		1100	18-08-1998		0.92	1210
2	04-05-2007	1.9	41	2400	21-04-1999	3.9	32	841
3	15-10-2007	2.4		2900				
4A	21-04-2008	2.9	74	3400 ^b				
4B	30-04-2008	3.1	96	–	03-05-1999	14	120	723
5	18-10-2008	3.3	99	3400	08-06-1999	16	130	717
					14-06-1999	16	130	717
					06-09-1999	24	200	661

^a day-month-year^b Measured on MJD 54564, 8 April 2008

Epochs 2 and 4B (04 May 2007 and 30 April 2008) correspond to the warm dust masses inferred by [Ev2020](#) on 21 April to 03 May 1999. The slight change between Epochs 4B and 5 might match the small increase between 03 May and 08 June 1999. By September 1999 [Ev2020](#) dust mass is 50% higher than the June values, but there are no more Spitzer observations with which to compare it. If the PAH absorption continued to grow at the rate of 0.44 yr^{-1} the $6.3\mu\text{m}$ PAH absorption feature would have been opaque ($\tau_{6.3} \approx 4$) by July 2016 when [Evans et al. \(2020\)](#) Sofia data were obtained and its non-detection is a consequence of high opacity, rather than noisier data.

9.2 Silicate coagulation in Epochs 3 to 5

The decreases in the astrosilicate absorption and consequent increases in the large grains of melilite might be a consequence of the coagulation of smaller astrosilicate dust into larger grains within the torus or PN. However, astrosilicate is assumed to be glassy whilst the large melilites are crystalline and a mechanism would be required to introduce crystallinity on a short timescale unless the astrosilicate already included a varied mixture of crystalline silicates with narrow bands that merge to form the assumed smooth $10\mu\text{m}$ absorption feature (see [Bowey & Adamson 2002](#)). This form of silicate dust is far more consistent with meteoritic and terrestrial materials than entirely amorphous dust.

Classic astrosilicates are also Mg-rich with between olivine and pyroxene stoichiometry $\sim\text{Mg}_{1.5}\text{SiO}_{3.5}$ (e.g. [Fogerty et al. 2016](#)) with 1.5 Mg atoms per Si atom, whilst the approximate stoichiometry of Si-rich melilite is $\text{Ca}_{1.5}\text{Mg}_{0.5}\text{SiO}_{3.5}$, i.e. 1.5 Ca atoms per Si atom and 3 Ca atoms for every Mg atom. In the diffuse medium the ratio of Ca to Mg atoms depleted from the gas into the dust is 8.4 per cent ([Snow & Witt 1996](#)). Hence, if the available Ca were entirely located in melilites up to 2.8 per cent of the silicate molecules or 2.5 per cent of the astrosilicate mass could have had melilite stoichiometry. This upper limit is similar to the 1.5–3 area per cent abundance of CAIs in chondritic meteorites and more than 80 per cent of the CAIs are formed of melilite or its alteration products (Section 3.2.2). It is also plausible that the melilites are the only coagulated components observed due to the strength of its overtone band which is 3 times that of other anhydrous crystalline silicates. I conclude that the astrosilicates may have clumped together to form the inferred melilites observed in the overtone features and that it is

plausible that grains like these were precursors to the melilite in the CAIs in meteorites.

10 CONCLUSIONS

The mid-infrared flux decreased during the period of the Spitzer observations. The 5.6 and $12.5\mu\text{m}$ fluxes decreased rapidly between April 2005 and May 2007, but the rate of change slowed between May 2007 and April 2008 and stopped between April and October 2008.

The proportion of optically-thin emission due to nanometre-sized SiC grains decreased between May 2007 and an apparent minimum in October 2007 which continued until 21 April 2008. The optically-thin proportion then increased rapidly in the 9 days to 30 April 2008 and then more slowly in the six months to October 2008.

The mass of cold carbonaceous dust increased. PAH absorption increased throughout the observations, with the rate accelerating between May 2007 and May 2008 and slowing down in the six months to October 2008. Increases in the abundance of $\lesssim 25\mu\text{m}$ -sized SiC grains in April 2008 might be significant but the data are not very sensitive to the overtone features before this time.

SiC formation mainly occurred before May 1999, followed by PAH formation in April–June 1999 once the dust was sufficiently cool. These grains are likely to be responsible for the growth in absorption due to PAH and $\lesssim 25\mu\text{m}$ -sized SiC dust between May 2007 and April 2008. The formation of large grains during the earlier period of mass loss and later optically-thin emission from 3nm -sized SiC is consistent with the hypothesis of [Speck, Thompson, & Hofmeister \(2005\)](#) that SiC grains are large in early phases when the mass-loss rate is low but that they become nm-sized when the infrared emission is optically thick and the stellar mass-loss rate is high.

Much of the dust responsible for the weak $10\mu\text{m}$ silicate absorption towards Sakurai’s Object is likely to be associated with Sakurai’s PN rather than interstellar in origin, because the optical-depth of the feature decreased between October 2007 and October 2008. Decreases in the astrosilicate absorption and increases in the large grains of melilite might be a consequence of the coagulation of smaller astrosilicate dust into larger grains within the torus or PN. Spectroscopic and Ca-abundance requirements are satisfied if up to 3 per cent of astrosilicate is converted to grains which produce melilite overtone features. It is plausible that grains like these were the pre-

cursors to the melilite in the CAIs in meteorites because more than 80 per cent of the CAIs are formed of melilite or its alteration products and the area per cent abundance of CAIs in chondritic meteorites is 1.5–3 per cent.

This study illustrates the importance of continued monitoring of mass-losing objects similar to Sakurai's Object in the mid-infrared. Intriguing results from this study are the appearance, growth and possible disappearance of the 6–7 μm absorption features and their use for the detection of PAHs and inference of 10 to 20 micron-sized melilite and SiC grains which are otherwise undetectable due to their high opacity in the 10 μm Si–O and Si–C stretching bands. The detection of melilite overtone absorption bands in circumstellar dust around oxygen-rich stars in the absence of H₂O ice and carbonaceous dust would be a priority, but it may be that the grains in these environments are too small and the grain-density too low to produce overtone features.

ACKNOWLEDGEMENTS

The author would like to thank the anonymous referee for insightful and careful reviews which have improved this paper. The author is supported by a 2-year *Science and Technology Research Council* Ernest Rutherford Returner Fellowship (ST/S004106/1). Spectra of SiC were supplied by A. M. Hofmeister. LR Spitzer spectra were obtained from the Combined Atlas of Sources with Spitzer/IRS Spectra (CASSIS), a product of the Infrared Science Center at Cornell University, supported by NASA and JPL. This work is based on observations made with the Spitzer Space Telescope, which is operated by the Jet Propulsion Laboratory, California Institute of Technology under a contract with NASA.

DATA STATEMENT

Data generated in this article will be shared on reasonable request to the corresponding author.

APPENDIX A: LABORATORY AND ASTRONOMICAL ABSORPTION PROFILES

A1 Hydrogenated Amorphous Carbon (HAC)

The mean optical depth profile of Sakurai's Object calculated in Section 4.2 is compared with various HAC samples synthesized by Grishko & Duley (2002) in Figure A1. HAC fails to match the 6.3 μm peak of Sakurai's Object due to excess absorption at 5.8 to 6.0 μm .

A2 Polycyclic Aromatic Hydrocarbons (PAHs)

Three spectra of well-characterised soot samples obtained by Carpentier et al. (2012) were compared with data for Sakurai's Object. Soot sample 3 (which is dominated by PAH units with many defects and twisted rings) provided the best match to observed 6–7 μm bands³. The laboratory sample consisted of agglomerated particles with diameters of ~ 30 nm. I removed narrow bands in the 5–8- μm region

³ Carpentier et al. found that the positions of these peaks matched the positions of class C aromatic infrared bands (AIBs) defined by Peeters et al. 2002 from emission bands observed in post-AGB objects (IRAS 13416 and CRL 2688), better than their other samples which had fewer defects.

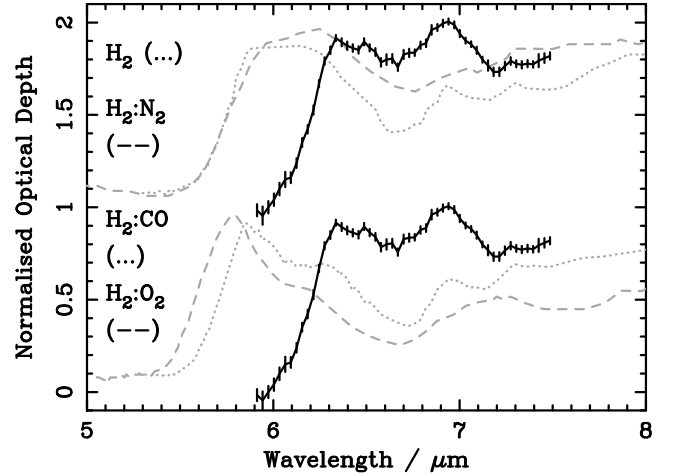


Figure A1. Comparison between digitized spectra of HAC samples (grey, arbitrary normalisation) synthesized by from graphite in various gas mixtures Grishko & Duley (2002) and the mean profile of Sakurai's Object (black) calculated in Section 4.2. The ratios of mixed gases during formation were 9:1. Fine structure below the resolution of the Spitzer spectra has been excluded.

due to H₂O vapour contamination in the spectrometer and a broader carbonyl -C=O band at 5.821 μm due to the use of oxygen in during sample preparation to produce the spectrum presented here.

Due to the inhomogeneous nature and undetermined particle thickness of the samples used for spectroscopy, Carpentier et al. wisely presented spectra with arbitrary optical depth scales. However, astrophysical studies require an estimate of the band strength using equation 4, $\kappa_{pk} = \tau_{pk}\rho L$, where ρ is the effective mass-density and L is the optical path length. Gavilan et al. (2017) used the same sooting apparatus to produce films with peaks near 6.3 μm with an optical depths $\tau \sim 0.07$ so I shall adopt this value. In a compressed sample ρ will be close to the density of the bulk solid. However, the soot particles are uncompressed and the effective mass is highly dependent on the degree of agglomeration and likely to be far less than that for a 'solid lump' of PAH ($\sim 1.8 \text{ gcm}^{-3}$). (Rissler et al. 2013) ascertained effective mass densities of soot of geometric diameters of 53–70 nm produced by a propane flame of $0.39\text{--}0.20 \text{ gcm}^{-3}$ based on a primary particle density of 1.8 gcm^{-3} . Hence, the value of κ_{pk} could be $1.3 \times 10^4 \text{ cm}^2\text{g}^{-1}$ ($\rho \approx 1.8 \text{ gcm}^{-3}$), $6 \times 10^4 \text{ cm}^2\text{g}^{-1}$ ($\rho \approx 0.39 \text{ gcm}^{-3}$) or $12 \times 10^4 \text{ cm}^2\text{g}^{-1}$ ($\rho \approx 0.2 \text{ gcm}^{-3}$). I adopt the primary particle size of 0.53 nm and density of 0.39 gcm^{-3} preferred by Rissler et al. (2013) giving $\kappa_{pk} = 6 \times 10^4 \text{ cm}^2\text{g}^{-1}$.

A3 Melilite, Hibonite and SiC

Normalised overtone spectra of compressed crystalline melilite and metamict hibonite powders (Bowie & Hofmeister 2005) are compared with the normalised spectrum of a $\sim 25 \mu\text{m}$ -thick wafer of β SiC (Hofmeister et al. 2009) in Figure A2.

The spectrum of a compressed powder is representative of the feature provided by a crystal of similar size because there are virtually no spaces between the grains, but orientational effects are lost; this is probably near to a lower limit for the melilite grain size because powder was added until the overtone was observed. The metamict hibonite overtone is broader than the melilite overtone due to a sub-peak at 6.3 μm . The band strength, κ_{pk} (6.9) of metamict hibonite is $0.48 \times 10^2 \text{ cm}^2\text{g}^{-1}$. Other hibonite overtones peak at 7.3 μm and

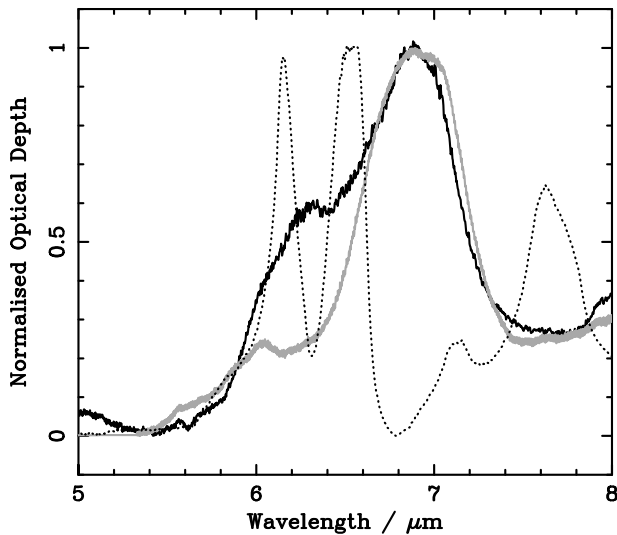


Figure A2. Comparison between melilite (grey), metamict hibonite (black) and β SiC overtones (dotted). Each spectrum is normalised to its largest peak.

have even weaker κ_{pk} of $0.08\text{--}0.14 \times 10^2 \text{cm}^2 \text{g}^{-1}$ and do not have any peaks at $6.9 \mu\text{m}$.

The $25 \mu\text{m}$ thickness of the SiC wafer is likely to be an upper size limit because larger grains are opaque, even in the overtones; see Hofmeister et al. (2009) for the spectrum of a $308 \mu\text{m}$ sample. Ideally a $20 \mu\text{m}$ wafer would have been measured because the $6.6 \mu\text{m}$ peak is slightly rounded, but this risked destruction of the specimen (Hofmeister, personal communication). Rounding of the peak and other artefacts occur in specimens which are opaque at the peak wavelength (see Hofmeister, Keppel, & Speck 2003). The nano- β SiC spectrum (Speck, Thompson, & Hofmeister 2005) is of a thin film of 97% purity consisting of 3 nm particles⁴, of thickness $0.34 \mu\text{m}$ (Hofmeister et al. 2009).

A4 Cyg OB2 no. 12

The shape of the interstellar silicate absorption feature in Figure 9(b) was derived from a CASSIS Spitzer LRS spectrum (AOR 27570176) calibrated by the method described in Section 2. Since the $8\text{--}13 \mu\text{m}$ spectrum was very similar to ground-based observations obtained by Bowey, Adamson, & Whittet (1998) and Bowey, Rawlings, & Adamson (2004), the continuum was estimated by scaling and extrapolating a continuum derived by Bowey, Rawlings, & Adamson (2004) to the wavelength-range of the Spitzer SL 1 spectrum. The resulting absorption profile was then normalised to unity at the peak wavelength ($9.75 \mu\text{m}$) and narrow lines (probably due to hydrogen emission local to the star) removed before comparison with Sakurai data. A detailed and different analysis of silicate dust in this line of sight has been published by Fogerty et al. (2016).

⁴ This is their tabulated value; in the text it says the grains were 20 nm ; values can be scaled accordingly

REFERENCES

- Abreu, N. M., Brearley, A. J. *Meteoritic & Planetary Science* 2005, 40, 609.
- Boogert A. C. A., Pontoppidan K. M., Knez C., Lahuis F., Kessler-Silacci J., van Dishoeck E. F., Blake G. A., et al., 2008, *ApJ*, 678, 985. doi:10.1086/533425
- Boogert A. C. A., Huard T. L., Cook A. M., Chiar J. E., Knez C., Decin L., Blake G. A., et al., 2011, *ApJ*, 729, 92. doi:10.1088/0004-637X/729/2/92
- Bouvier, A., Meenakshi, W. 2010, *Nature Geoscience*, 3, 637.
- Bowey, J. E., Hofmeister, A. M. 2005, *MNRAS*, 358, 1383
- Bowey, J. E., Adamson A. J. 2002, *MNRAS*, 334, 94
- Bowey J. E., Rawlings M. G., Adamson A. J., 2004, *MNRAS*, 348, L13. doi:10.1111/j.1365-2966.2004.07497.x
- Bowey J. E., Adamson A. J., Whittet D. C. B., 1998, *MNRAS*, 298, 131. doi:10.1046/j.1365-8711.1998.01640.x
- Carpentier Y., Féraud G., Dartois E., Brunetto R., Charon E., Cao A.-T., d'Hendecourt L., et al., 2012, *A&A*, 548, A40. doi:10.1051/0004-6361/201118700
- Chesneau O., Clayton G. C., Lykou F., De Marco O., Hummel C. A., Kerber F., Lagadec E., et al., 2009, *A&A*, 493, L17. doi:10.1051/0004-6361:200811173
- Cohen M., Barlow M. J., Liu X.-W., Jones A. F., 2002, *MNRAS*, 332, 879. doi:10.1046/j.1365-8711.2002.05350.x
- Duerbeck H. W., Benetti S., 1996, *ApJL*, 468, L111. doi:10.1086/310241
- Evans A., Gehrz R. D., Woodward C. E., Banerjee D. P. K., Geballe T. R., Clayton G. C., Sarre P. J., et al., 2020, *MNRAS*, 493, 1277. doi:10.1093/mnras/staa343
- Evans A., Tyne V. H., van Loon J. T., Smalley B., Geballe T. R., Gehrz R. D., Woodward C. E., et al., 2006, *MNRAS*, 373, L75. doi:10.1111/j.1745-3933.2006.00246.x
- Evans A., Geballe T. R., Smalley B., Tyne V. H., Eyres S. P. S., 2002, *A&A*, 394, 971. doi:10.1051/0004-6361:20021229
- Eyres S. P. S., Evans A., Geballe T. R., Salama A., Smalley B., 1998, *MNRAS*, 298, L37. doi:10.1046/j.1365-8711.1998.01898.x
- Fogerty S., Forrest W., Watson D. M., Sargent B. A., Koch I., 2016, *ApJ*, 830, 71. doi:10.3847/0004-637X/830/2/71
- Gavilan L., Le K. C., Pino T., Alata I., Giuliani A., Dartois E., 2017, *A&A*, 607, A73. doi:10.1051/0004-6361/201730712
- Geballe T. R., Evans A., Smalley B., Tyne V. H., Eyres S. P. S., 2002, *Ap&SS*, 279, 39
- Grishko V. I., Duley W. W., 2002, *ApJ*, 568, 448. doi:10.1086/338926
- Helling C., Jorgensen U. G., Plez B., Johnson H. R., 1996, *A&A*, 315, 194
- Hezel D. C., Russell S. S., Ross A. J., Kearsley A. T., 2008, *M&PS*, 43, 1879. doi:10.1111/j.1945-5100.2008.tb00649.x
- Hinkle K. H., Joyce R. R., 2014, *ApJ*, 785, 146. doi:10.1088/0004-637X/785/2/146
- Hinkle K. H., Joyce R. R., Matheson T., Lacy J. H., Richter M. J., 2020, *ApJ*, 904, 34. doi:10.3847/1538-4357/abbd9a
- Hofmeister A. M., Wopenka B., Locock A. J., 2004, *Geochim. Cosmochim. Acta*, 68, 4485.
- Hofmeister A. M., Keppel E., Speck A. K., 2003, *MNRAS*, 345, 16. doi:10.1046/j.1365-8711.2003.06899.x
- Hofmeister A. M., Pitman K. M., Goncharov A. F., Speck A. K., 2009, *ApJ*, 696, 1502. doi:10.1088/0004-637X/696/2/1502
- Hoppe P., Amari S., Zinner E., Ireland T., Lewis R. S., 1994, *ApJ*, 430, 870. doi:10.1086/174458
- Houck J. R., Roellig T. L., van Cleve J., Forrest W. J., Herter T., Lawrence C. R., Matthews K., et al., 2004, *ApJS*, 154, 18. doi:10.1086/423134
- IRS Instrument Team & Science User Support Team, Version 5.0, S18.18 December 2011 title: IRS Instrument Handbook. <https://irsa.ipac.caltech.edu/data/SPITZER/docs/irs/irsinstrumenthandbook/>.
- Keane J. V., Tielens A. G. G. M., Boogert A. C. A., Schutte W. A., Whittet D. C. B., 2001, *A&A*, 376, 254. doi:10.1051/0004-6361:20010936
- Morlok, A., Koehler, M., Grady, M. M. 2008, *Meteoritics & Planetary Science* 43, 1147
- Molster F. J., Lim T. L., Sylvester R. J., Waters L. B. F. M., Barlow M. J., Beintema D. A., Cohen M., et al., 2001, *A&A*, 372, 165. doi:10.1051/0004-6361:20010465

- Lebouteiller, V., Barry, D. J., Spoon, H.W.W., Bernard-Salas, J., Sloan, G.C., Houck, J.R., Weedman, D., 2011 *ApJS*, 196, 8
- Nakano S., Sakurai Y., Hazen M., McNaught R. H., Benetti S., Duerbeck H. W., Cappellaro E., et al., 1996, *IAUC*, 6322
- Peeters E., Hony S., Van Kerckhoven C., Tielens A. G. G. M., Allamandola L. J., Hudgins D. M., Bauschlicher C. W., 2002, *A&A*, 390, 1089. doi:10.1051/0004-6361:20020773
- Pino T., Dartois E., Cao A.-T., Carpentier Y., Chamail  T., Vasquez R., Jones A. P., et al., 2008, *A&A*, 490, 665. doi:10.1051/0004-6361:200809927
- Pollacco D., 1999, *MNRAS*, 304, 127. doi:10.1046/j.1365-8711.1999.02300.x
- Rissler J., Messing M. E., Malik A. I., Nilsson P. T., Nordin E. Z., Bohgard M., Sanati M., et al., 2013, *AerST*, 47, 792. doi:10.1080/02786826.2013.791381
- Rubin A. E., Ma C., 2017, *Chemie der Erde Geochemistry*, 77, 325. doi:10.1016/j.chemer.2017.01.005
- Snow T. P., Witt A. N., 1996, *ApJL*, 468, L65. doi:10.1086/310225
- Speck A. K., Thompson G. D., Hofmeister A. M., 2005, *ApJ*, 634, 426. doi:10.1086/496955
- Tyne V. H., Evans A., Geballe T. R., Eyres S. P. S., Smalley B., Duerbeck H. W., 2002, *MNRAS*, 334, 875. doi:10.1046/j.1365-8711.2002.05561.x
- Werner M. W., Roellig T. L., Low F. J., Rieke G. H., Rieke M., Hoffmann W. F., Young E., et al., 2004, *ApJS*, 154, 1. doi:10.1086/422992
- Whittet D. C. B., 2003, *Dust in the Galactic Environment* (21 Oct. 2002). Bristol ; Philadelphia : IOP 2nd ed. ISBN : 0750306246.
- Whittet D. C. B., Duley W. W., Martin P. G., 1990, *MNRAS*, 244, 427
- Zhang M., Bonato E., King A. J., Russell S. S., Tang G., Lin Y., 2020, *M&PS*, 55, 911. doi:10.1111/maps.13473

This paper has been typeset from a $\text{\TeX}/\text{\LaTeX}$ file prepared by the author.